Editors' Suggestion

# Biased Ensembles of Pulsating Active Matter

William D. Piñeros and Étienne Fodor
*Department of Physics and Materials Science, University of Luxembourg, L-1511 Luxembourg, Luxembourg*

(Received 23 April 2024; revised 2 December 2024; accepted 20 December 2024; published 23 January 2025)

We discover unexpected connections between packing configurations and rare fluctuations in dense systems of active particles subject to pulsation of size. Using large deviation theory, we examine biased ensembles which select atypical realizations of the dynamics exhibiting high synchronization in particle size. We show that the order emerging at high bias can manifest as distinct dynamical states featuring high to vanishing pulsation current. Remarkably, transitions between these states arise from changing the system geometry at fixed bias and constant density. We rationalize such transitions as arising from the change in packing configurations which, depending on box geometry, may induce highly ordered or geometrically frustrated structures. Furthermore, we reveal that a master curve in the unbiased dynamics, correlating polydispersity and current, helps predict the dynamical state emerging in the biased dynamics. Finally, we demonstrate that deformation waves can propagate under suitable geometries when biasing with local order.

DOI: 10.1103/PhysRevLett.134.038301

*Introduction*—Active matter encompasses systems which constantly dissipate energy to sustain collective behaviors far from equilibrium. For instance, assemblies of self-propelled particles (SPPs) [1–3] yield nonequilibrium phenomena which have been extensively studied, such as a polarized collective motion [4,5] and a phase separation without attractive interactions [6,7]. Energy dissipation can also take other forms beyond motility, opening the door to novel physics beyond that of SPPs. For instance, in some biological tissues (e.g., epithelial [8], cardiac [9], and uterine [10] tissues), each cell can sustain periodic changes of shape, leading to the propagation of deformation waves. A recent model of pulsating active matter (PAM) has captured such waves in terms of densely packed particles whose sizes constantly pulsate [11]. In contrast with other models of deforming particles where waves have not been observed [12–15], PAM relies on synchronizing nearby sizes [11,16–19]. In the absence of any synchronizing interaction, it is largely unclear under which conditions deformation waves could still potentially emerge.

Biased ensembles (BEs) offer the perfect toolbox [20] to search for waves in nonsynchronizing PAM. Building on large deviation theory [21], BEs select the rare trajectories which (i) achieve some atypical statistics of a chosen observable while (ii) deviating the least from the original, unbiased dynamics. In practice, BEs do not presume *how* the system should accommodate the constraints (i) and (ii). At a sufficiently large bias, the dynamics are given enough play to explore novel configurations, potentially yielding dynamical phase transitions [22–24]. Rare trajectories can actually be mapped into an effective dynamics [25–28], which constitute the optimal mechanism for stabilizing the phases selected by BEs. This connection between optimal control and large deviations has inspired novel strategies for material design [29,30].

In active matter, BEs have already been used to unravel novel mechanisms for promoting collective effects [31]. For instance, in large deviations of SPPs [32–34], BEs have revealed that alignment effectively emerges from avoiding

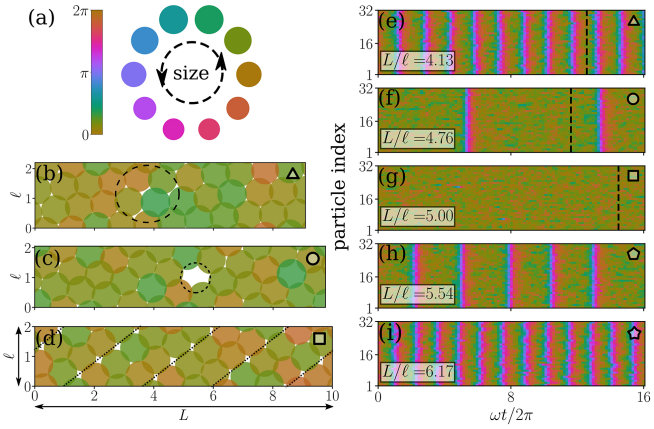


FIG. 1. (a) Size of particles subject to a periodic pulsation controlled by an internal phase. In biased ensembles at high density, changing the box aspect ratio $L/\ell$ with sides $\{\ell, L\}$ results in various configurations with either (b) defects, (c) voids, or (d) regular structures. These correspond, respectively, to varying collective states for different $L/\ell$: (e),(i) cycles with periodic size change, (f),(h) intermittent behavior with aperiodic size change, and (g) arrest where particle repulsion yields a uniform frozen size. Particles are indexed per increasing position along the $L$ axis. Dashed lines refer to the snapshots shown in (b)–(d), and symbols indicate parameter values in Fig. 3.

 

collisions between nearby particles, yielding collective motion [35–37]. These results are reminiscent of the collective behaviors emerging in some models of SPPs without alignment [38–40] and stand in contrast with standard flocking models which require *ad hoc* aligning rules [5]. In a similar fashion, it is tempting to examine whether BEs of nonsynchronizing PAM entail unexpected transitions, potentially uncovering novel pathways toward wave formation.

In this Letter, we investigate the collective dynamics in BEs of dense assemblies of pulsating particles in a two-dimensional box (Fig. 1). Starting from configurations without any synchronization, we reveal how biasing with a global order parameter promotes transitions toward various homogeneous states: cycles, arrest, and intermittent behavior. Remarkably, the packing constraint imposed by the box geometry, which restricts the unbiased configurations and, hence, its fluctuations, also selects for one of the three ordered states under bias. Specifically, we show that slight variations in the unbiased statistics of some relevant observables allow one to anticipate the emergence of transitions in the biased dynamics. Finally, we reveal that deformation waves can be stabilized for specific geometries when biasing with a local order parameter. Overall, our results demonstrate that, at fixed bias and constant density, controlling the box geometry is a novel route toward unexpected phase transitions in BEs of PAM.

*Pulsating active matter: The role of box geometry*—We consider a two-dimensional system of pulsating particles (Fig. 1) whose sizes change as

$$\sigma_i = \frac{\sigma_0}{2}\frac{1+\lambda\sin\theta_i}{1+\lambda}, \tag{1}$$

where $\sigma_0 = 1$ is the base size, $\theta_i$ the internal phase of particle $i$, and $\lambda = 0.05$ the pulsation amplitude. The particles follow overdamped Langevin dynamics:

$$\dot{\mathbf{r}}_i = -\mu_r \partial_{\mathbf{r}_i} V + \sqrt{2D_r}\boldsymbol{\xi}_i, \tag{2}$$

$$\dot{\theta}_i = \omega - \mu_\theta \partial_{\theta_i} V + \sqrt{2D_\theta}\eta_i. \tag{3}$$

The potential $V = \sum_{i,j<i} U(a_{ij})$ depends on the scaled distance $a_{ij} = |\mathbf{r}_j - \mathbf{r}_i|/(\sigma_i + \sigma_j)$, and $(\boldsymbol{\xi}_i, \eta_i)$ are uncorrelated Gaussian white noises with unit correlations. The phase drift is constant and set to $\omega = 10$. The diffusion coefficients $D_{r/\theta}$ and mobilities $\mu_{r/\theta}$ follow the fluctuation-dissipation relation ($D_r/\mu_r = D_\theta/\mu_\theta = T$) and are set to unity. Then, in the absence of drift ($\omega = 0$), the system follows an equilibrium dynamics which relaxes to the Boltzmann distribution $P \sim e^{-V/T}$. Interactions follow volume exclusion via a Weeks-Chandler-Anderson potential $U(a) = U_0(a^{-12} - 2a^{-6})$ with $U_0 = 1$ and cutoff set at $a = 1$. In contrast with [11], we do not consider here any synchronizing interaction between phases. In what follows, we run simulations with periodic boundary conditions for $N = 32$ particles at density $\rho = 1.6$ (unless stated otherwise), and we examine how the box aspect ratio $L/\ell$ (Fig. 1) impacts the emerging dynamics.

We start by evaluating the global order parameter quantifying phase synchronization across the system:

$$\phi_{\mathrm{gb}} = \frac{1}{N}\left|\sum_{j=1}^{N} e^{i\theta_j}\right| = \frac{1}{N}\sqrt{\sum_{i,j=1}^{N}\cos(\theta_i - \theta_j)}. \tag{4}$$

Configurations with a nearly uniform size distribution have $\phi_{\mathrm{gb}} \simeq 1$, whereas those with high polydispersity have $\phi_{\mathrm{gb}} \simeq 0$. Despite the absence of any synchronizing interaction, our simulations exhibit a moderate ordering of particle sizes [Fig. 2(a)]. Indeed, the repulsion term in Eq. (3) constrains the sizes to fluctuate around a preferred value. This effect is captured at mean-field level by approximating $\partial_{\theta_i} V \approx (\partial_\varphi V)(\partial_{\theta_i}\varphi)$ [11]. The coefficient $\partial_\varphi V$ increases with $\rho$, and the packing fraction $\varphi = (\pi\rho/N)\sum_i \sigma_i^2$ admits the same local minimum for each $\theta_i \in [0, 2\pi]$, thus favoring order at high $\rho$.

Interestingly, we observe that $\langle\phi_{\mathrm{gb}}\rangle$ (where $\langle\cdot\rangle$ indicates average over realizations) strongly varies with the aspect ratio $L/\ell$, with a maximum at $L/\ell \simeq 5$ [Fig. 2(a)], showing that one can actually enhance order by appropriately tuning the box geometry. We find that such a variation with $L/\ell$ wanes gradually for larger $N$ at fixed $\rho$ but remains noticeable even for systems with $N \simeq 10^2$ (see Fig. S2 in [41]). The enhancement of order is accompanied by a dynamical slowdown, as indicated by the reduction of the average phase current [Fig. 2(b)]:

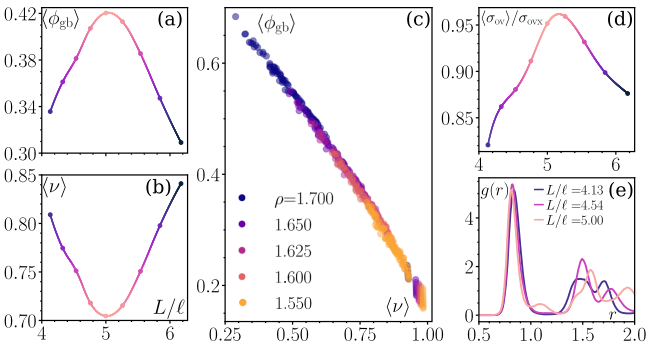


FIG. 2. (a),(b) Global order $\langle\phi_{\mathrm{gb}}\rangle$ and phase current $\langle\nu\rangle$ as functions of the aspect ratio $L/\ell$. Lines are guides to the eye. (c) Correlation between global order $\langle\phi_{\mathrm{gb}}\rangle$ and phase current $\langle\nu\rangle$ for various densities $\rho = N/(L\ell)$, changing both $L/\ell$ and the particle number $N$. (d) Average overlap $\langle\sigma_{\mathrm{ov}}\rangle$, relative to that of hexagonal packing $\sigma_{\mathrm{ovx}}$ at the same density, for varying values of $L/\ell$. (e) Radial distribution $g$ as a function of the interparticle distance $r$. Line colors in (b), (d), and (e) as per the value of $\langle\phi_{\mathrm{gb}}\rangle$ in (a).

$$\nu = \frac{1}{N\omega t}\sum_{i=1}^{N}\int_0^t dt'\dot{\theta}_i(t'). \tag{5}$$

Similar results hold for other box ratios and particle numbers; see Fig. S5 in [41]. In fact, plotting $\langle\phi_{\rm gb}\rangle$ against $\langle\nu\rangle$ for different values of $N$, $L/\ell$, and $\rho$ results in a master curve, where increasing order systematically correlates with decreasing current [Fig. 2(c)]. Interestingly, some of the curves, shown in Fig. 2(c) for different $\rho$, overlap. Indeed, for some combinations of $N$ and $L/\ell$, systems at various $\rho$ can experience an equivalent average repulsion, yielding a similar set of values for $\langle\phi_{\rm gb}\rangle$ and $\langle\nu\rangle$.

We can rationalize these results from a packing perspective. To this end, we explore how repulsion varies for different values of $L/\ell$ by computing the average overlap:

$$\langle\sigma_{\rm ov}\rangle = \frac{2}{N(N-1)}\sum_{i,j\in\partial_i}\langle\sigma_i+\sigma_j-|\mathbf{r}_i-\mathbf{r}_j|\rangle, \tag{6}$$

where the sum runs over particles for which $\sigma_i+\sigma_j > |\mathbf{r}_i-\mathbf{r}_j|$. We find the average overlap peaks at $L/\ell \simeq 5$ [Fig. 2(d)], which coincides with the maximum of $\langle\phi_{\rm gb}\rangle$ and the minimum of $\langle\nu\rangle$ [Figs. 2(a) and 2(b)]. Interestingly, $\langle\sigma_{\rm ov}\rangle$ is comparable to the overlap $\sigma_{\rm ovx}$ of a hexagonal packing at the same density (Appendix A), and a regular structure can be identified at $L/\ell \simeq 5$; see Sec. I A in [41]. These results indicate that higher overlap (hence, repulsion) induce more regular arrangements, corresponding to lower polydispersity and lower pulsation current in the system. To illustrate further the relation between structure and box geometry, we evaluate the radial distribution function (rdf)

$$g(r) = \frac{1}{\rho}\sum_{i,j\neq i}\langle\delta(r-|\mathbf{r}_i-\mathbf{r}_j|)\rangle \tag{7}$$

and observe that indeed density correlations change drastically for varying $L/\ell$ [Fig. 2(e)]. In particular, the rdf for $L/\ell = 5$ features a secondary peak at $r \simeq 1.1$ not present for other values of $L/\ell$, which hints at qualitative differences between the corresponding packing structures. A similar dependence of structure on box geometry has been reported in systems of monodisperse, passive particles [45–47].

In short, our findings show that changing the box geometry alters the packing structure assumed by pulsating particles, which, in turn, provides a route to controlling order and current at fixed density.

*Ensembles biased by global order: Cycles and arrest*—We study the large deviations of the dynamics with respect to $\phi_{\rm gb}$ [Eq. (4)]. In particular, we seek trajectories for which the time average

$$\bar{\phi}_{\rm gb} = \frac{1}{t_o}\int_0^{t_o}\phi_{\rm gb}(t)dt \tag{8}$$

displays atypically large values at large observation time $t_o$. To this end, we use a BE selecting for such trajectories through rare realizations of the noise terms in Eqs. (2) and (3). Chiefly, we denote averages with respect to this BE as

$$\langle\cdot\rangle_{\rm gb} = \frac{\langle\cdot e^{-sNt_o\bar{\phi}_{\rm gb}}\rangle}{\langle e^{-sNt_o\bar{\phi}_{\rm gb}}\rangle}. \tag{9}$$

The bias strength $s$ effectively controls the statistics of $\bar{\phi}_{\rm gb}$. At vanishing bias, $s = 0$, one recovers the ensemble of the original dynamics: $\langle\cdot\rangle_{\rm gb} = \langle\cdot\rangle$. In this work, we implement the trajectory selection via a cloning algorithm using population dynamics [48]. It consists in simulating $n_c$ identical (though distinctly seeded) parallel runs, which are regularly replicated or pruned through a sampling procedure parametrized by $s$. In the limit of large $n_c$ and large $t_o$, this procedure converges to a BE whose trajectories represent the least unlikely dynamics to stabilize the desired atypical statistics of $\bar{\phi}_{\rm gb}$.

For large $N$, numerical convergence becomes increasingly challenging [20]. Generally, a useful method consists in adding some terms in the dynamics which effectively approximate trajectory selection and improves convergence [20,35,36,49,50]. Here, we consider fully connected synchronizing interactions:

$$\dot{\theta}_i = \omega - \mu_\theta\partial_{\theta_i}V + \varepsilon\sum_{j=1}^{N}\sin(\theta_j-\theta_i) + \sqrt{2D_\theta}\eta_i. \tag{10}$$

We adapt our numerical selection of trajectories [41] to ensure that, while using the dynamics in Eq. (10), we still sample the proper BE [Eq. (9)] defined independently of synchronizing interactions. Furthermore, for each run, we heuristically adjust the amplitude $\varepsilon$ throughout the trajectory [41], which converges at large $t_0$ to a value determined by $s$. In what follows, we are interested in the regime of bias which promotes order, namely, atypically large $\bar{\phi}_{\rm gb}$, corresponding here to $s < 0$ and $\varepsilon > 0$.

Starting from the unbiased configuration with highest $\langle\phi_{\rm gb}\rangle$ and lowest $\langle\nu\rangle$, namely, for $L/\ell \simeq 5$ [Figs. 2(a) and 2(b)], increasing $|s|$ yields a highly ordered state without phase current: $\langle\phi_{\rm gb}\rangle_{\rm gb} \simeq 1$ and $\langle\nu\rangle_{\rm gb} \simeq 0$ [Figs. 3(a) and 3(b)]. Such a configuration is analogous to the arrested state previously reported in synchronizing PAM [11,17]. Remarkably, considering an unbiased configuration at the tail of the curve $\langle\nu\rangle$ vs $L/\ell$ [Fig. 2(b)], increasing $|s|$ now yields an ordered state with nonvanishing averaged current [Figs. 3(a) and 3(b)], which is reminiscent of the cycling state in synchronizing PAM [11,17]. Therefore, the box geometry not only impacts the unbiased dynamics of nonsynchronizing PAM, it also strongly influences its rare

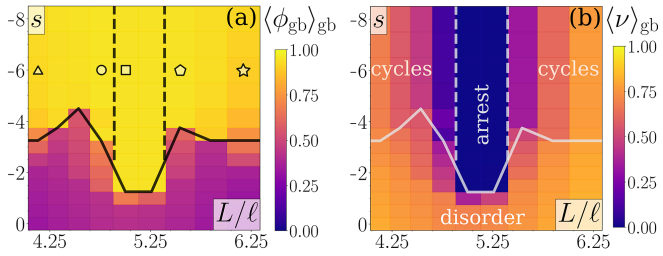


FIG. 3. Phase diagram in ensembles biased by global order [Eq. (9)] in terms of the bias strength $s$ and the aspect ratio $L/\ell$: (a) global order $\langle\phi_{gb}\rangle_{gb}$ and (b) phase current $\langle\nu\rangle_{gb}$. Boundary lines are for $\langle\phi_{gb}\rangle_{gb} = 0.65$ (solid) and $\langle\nu\rangle_{gb} = 0.1$ (dashed). Markers refer to various trajectories at $s = -6$, as shown in Fig. 1.

fluctuations, yielding two different types of ordered states.

Varying $L/\ell$ at constant $|s| > 4.5$, the transition between cycling and arrest [Fig. 3(b)] mirrors the slowdown of the unbiased dynamics [Fig. 2(b)]. Again, this result can be rationalized from a packing perspective. Specifically, arrest is associated with a regular packing [Fig. 1(d)] which impedes the periodic expansion and contraction of particles [Fig. 1(g)], whereas cycles have a defective packing [Fig. 1(b)] which facilitates global changes in particle sizes [Figs. 1(e) and 1(i)]. Note that $\langle\phi_{gb}\rangle_{gb}$ is slightly higher for arrest compared with cycles [Fig. 3(a)], so that regular packing is associated with a reduced polydispersity, as in the unbiased case (Fig. 2). Interestingly, we also observe an intermittent dynamics with aperiodic size changes [Figs. 1(f) and 1(h)] whose packing contains motile voids [Fig. 1(c)]. Indeed, measurements of structural order clearly highlight structural differences between each one of these dynamical states; see Appendix B and Fig. S4 in [41].

Overall, our results for $(N, \rho) = (32, 1.6)$ show that packing configurations, imposed by the box geometry, impact both unbiased and biased dynamics. Importantly, we reveal that the unbiased statistics actually allows one to anticipate how the system orders as a function of $L/\ell$ in our BE. We find a similar effect is generically observed for other values of $(N, \rho)$; for instance, see the phase diagram for $(N, \rho) = (26, 1.6)$ in Fig. S5 of [41].

*Ensembles biased by local order: Deformation waves*—In synchronizing PAM [11,17], deformation waves emerge as a competition between arrest and cycling. Given that in nonsynchronizing PAM the BE promoting global order [Eq. (9)] yields arrest and cycles (Fig. 3), it is intriguing to understand what class of BE may also induce deformation waves. To this end, we introduce the local order parameter

$$\phi_{lc} = \frac{1}{N}\sum_{i=1}^{N}\sum_{j=1}^{n_i}\frac{\cos(\theta_j - \theta_i)}{n_i}, \tag{11}$$

where $n_i$ is the number of neighbors in contact with particle $i$, and the corresponding biased average

$$\langle\cdot\rangle_{lc} = \frac{\langle\cdot e^{-sNt_o\bar{\phi}_{lc}}\rangle}{\langle e^{-sNt_o\bar{\phi}_{lc}}\rangle}, \qquad \bar{\phi}_{lc} = \frac{1}{t_o}\int_0^{t_o}\phi_{lc}(t)dt. \tag{12}$$

To improve sampling, we now consider *locally* synchronizing interactions:

$$\dot{\theta}_i = \omega - \mu_\theta\partial_{\theta_i}V + \varepsilon\sum_{j=1}^{n_i}\sin(\theta_j - \theta_i) + \sqrt{2D_\theta}\eta_i. \tag{13}$$

In practice, Eq. (13) enhances convergence for the BE in Eq. (12) at moderate $|s|$, while Eq. (10) actually works better for the same BE at large $|s|$. At each $s$, we systematically compare results obtained by employing either type of interaction (i.e., with local or global synchronization) and select the ones with optimal convergence [41].

Interestingly, for values of $L/\ell$ coincident with the minimum of $\langle\nu\rangle$ [Fig. 2(b)], we observe again the emergence of an arrested state with local and global order [Figs. 4(a) and 4(b)] comparable to the results from the previous BE [Eq. (3)]. In contrast, for $L/\ell$ sufficiently far away from the minimum of $\langle\nu\rangle$, phase ordering now occurs through two distinct states. As $|s|$ increases, local order increases with negligible change in global order, i.e., $\langle\phi_{lc}\rangle_{lc} > \langle\phi_{lc}\rangle$ and $\langle\phi_{gb}\rangle_{lc} \simeq \langle\phi_{gb}\rangle$. In this state, particle sizes cycle periodically in a locally coordinated way, yielding the spontaneous emergence of deformation waves [Figs. 4(d) and 4(e)] not present in the unbiased dynamics [Fig. 4(c)]. For higher $|s|$, the range of particle coordination increases, which increases global order ($\langle\phi_{gb}\rangle_{lc} > \langle\phi_{gb}\rangle$) and ultimately results in a cycling state [Fig. 4(f)] similar to that of the previous BE [Fig. 1(e)].

In this manner, the BE promoting local order [Eq. (12)] reproduces all the states of synchronizing PAM [11,17]: disorder, arrest, cycles, and waves. Furthermore, waves arise only for box sizes $L$ accommodating at least one wavelength. As the wavelength increases with $|s|$, waves are stable only over a finite range of $s$. As such, waves can be seen as precursory to cycles. In contrast, arrest does not display such a gradual ordering from local to global but rather directly emerges from disorder at comparatively low bias. Moreover, the critical $s$ for this transition is almost unchanged when biasing with either global [Fig. 3(a)] or local [Fig. 4(b)] order.

In short, our results demonstrate that waves spontaneously emerge as a strategy to promote high *local* order while maintaining only moderate *global* order. Again, the box geometry plays a crucial role here. Specifically, for values of $L/\ell$ promoting regular packing configurations, local deformations are strongly hampered, so that arrest is more stable than waves for any $s < 0$.

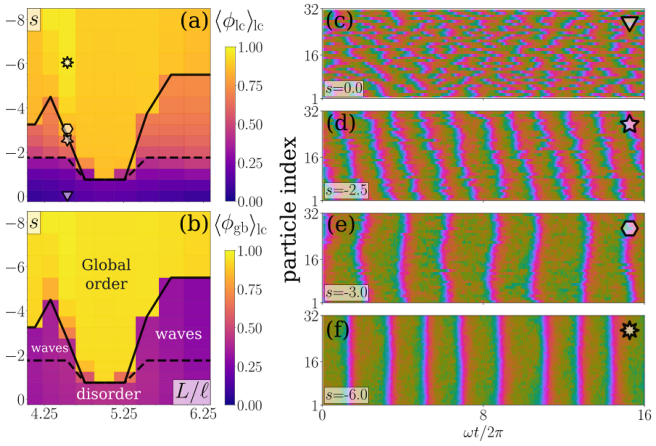


FIG. 4. Phase diagram in ensembles biased by local order [Eq. (12)] in terms of the bias strength $s$ and the aspect ratio $L/\ell$: (a) local order $\langle\phi_{\rm lc}\rangle_{\rm lc}$ and (b) global order $\langle\phi_{\rm gb}\rangle_{\rm lc}$. Boundary lines are for $\langle\phi_{\rm lc}\rangle_{\rm lc} = 0.65$ (solid) and $\langle\phi_{\rm gb}\rangle_{\rm lc} = 0.45$ (dashed). Markers refer to various trajectories at $L/\ell = 4.53$: (c) disorder, (d), (e) waves, and (f) cycles.

*Discussion*—We reveal some unexpected connections between packing configurations and rare fluctuations in dense systems of pulsating particles. The box geometry is a proxy to controlling the packing structure, with dramatic consequences on collective effects. Specifically, we show that one can induce transitions between two types of ordered states in BEs, either with or without current, simply by changing the box geometry. Arrest is associated with regular packing configurations where the particle repulsion exactly counteracts their pulsation. On the other hand, when the box geometry induces a defective packing, it generates regions of inhomogeneous repulsion that ultimately lead to cycling. Remarkably, the transitions between arrest and cycles in the biased dynamics can actually be anticipated from the statistics of current and order in the unbiased dynamics.

Our transitions bring interesting parallels with the emergence of arrest in other dense systems. In densely packed SPPs, structural defects destabilize arrest [51], alter the glass transition [52], and induce intermittent plastic yielding [53]. The mechanical properties of such systems can actually be related to those of sheared granular systems [54]. Moreover, local growth of deforming particles also results in dynamical heterogeneities resembling sheared glasses [55]. These examples suggest that a generic mechanism may explain how activity controls the transitions between arrested and fluidized states. Remarkably, even in the absence of shear, allowing size fluctuations shifts the glass transition to lower temperatures [56–59], illustrating how local deformation helps relax the dynamics near arrest [60].

Our approach could also motivate further studies in other active models where synchronization yields patterns [61–63]. For instance, considering BEs with local or global order could help delineate minimal conditions to stabilize patterns, similarly to how waves emerge only for specific box geometries in our case. To improve sampling, one could rely on more complex interactions beyond the synchronization considered here. To this end, recent methods inspired by machine learning provide a rich toolbox [64–66] which could prove quite useful.

*Acknowledgments*—We acknowledge insightful discussions with Y.-E. Keta and R. L. Jack. Work was funded by the Luxembourg National Research Fund (FNR), Grant Reference No. 14389168, and the Marie Skłodowska-Curie Grant No. 101104945.

*Data availability*—Supporting data and code are freely available, respectively, in the Zenodo data repository [67] and Github [68].

[1] M. C. Marchetti, J. F. Joanny, S. Ramaswamy, T. B. Liverpool, J. Prost, M. Rao, and R. A. Simha, Hydrodynamics of soft active matter, Rev. Mod. Phys. **85**, 1143 (2013).
[2] C. Bechinger, R. Di Leonardo, H. Löwen, C. Reichhardt, G. Volpe, and G. Volpe, Active particles in complex and crowded environments, Rev. Mod. Phys. **88**, 045006 (2016).
[3] É. Fodor and M. C. Marchetti, The statistical physics of active matter: From self-catalytic colloids to living cells, Physica (Amsterdam) A **504**, 106 (2018).
[4] T. Vicsek, A. Czirók, E. Ben-Jacob, I. Cohen, and O. Shochet, Novel type of phase transition in a system of self-driven particles, Phys. Rev. Lett. **75**, 1226 (1995).
[5] H. Chaté, Dry aligning dilute active matter, Annu. Rev. Condens. Matter Phys. **11**, 189 (2020).
[6] Y. Fily and M. C. Marchetti, Athermal phase separation of self-propelled particles with no alignment, Phys. Rev. Lett. **108**, 235702 (2012).
[7] M. E. Cates and J. Tailleur, Motility-induced phase separation, Annu. Rev. Condens. Matter Phys. **6**, 219 (2015).
[8] A. Bailles, E. W. Gehrels, and T. Lecuit, Mechanochemical principles of spatial and temporal patterns in cells and tissues, Annu. Rev. Cell Dev. Biol. **38**, 321 (2022).
[9] A. Karma, Physics of cardiac arrhythmogenesis, Annu. Rev. Condens. Matter Phys. **4**, 313 (2013).
[10] K. M. Myers and D. Elad, Biomechanics of the human uterus, WIREs Syst. Biol. Med. **9**, e1388 (2017).
[11] Y. Zhang and E. Fodor, Pulsating active matter, Phys. Rev. Lett. **131**, 238302 (2023).
[12] E. Tjhung and T. Kawasaki, Excitation of vibrational soft modes in disordered systems using active oscillation, Soft Matter **13**, 111 (2017).
[13] E. Tjhung and L. Berthier, Discontinuous fluidization transition in time-correlated assemblies of actively deforming particles, Phys. Rev. E **96**, 050601(R) (2017).
[14] N. Oyama, T. Kawasaki, H. Mizuno, and A. Ikeda, Glassy dynamics of a model of bacterial cytoplasm with metabolic activities, Phys. Rev. Res. **1**, 032038(R) (2019).

[15] Y. Koyano, H. Kitahata, and A. S. Mikhailov, Diffusion in crowded colloids of particles cyclically changing their shapes, Europhys. Lett. **128**, 40003 (2019).
[16] Y. Togashi, Modeling of nanomachine/micromachine crowds: Interplay between the internal state and surroundings, J. Phys. Chem. B **123**, 1481 (2019).
[17] A. Manacorda and E. Fodor, Diffusive oscillators capture the pulsating states of deformable particles, arXiv:2310.14370.
[18] W. hua Liu, W. jing Zhu, and B. quan Ai, Collective motion of pulsating active particles in confined structures, New J. Phys. **26**, 023017 (2024).
[19] Z.-Q. Li, Q.-L. Lei, and Y. qiang Ma, Fluidization and anomalous density fluctuations in epithelial tissues with pulsating activity, arXiv:2402.02981.
[20] R. L. Jack, Ergodicity and large deviations in physical systems with stochastic dynamics, Eur. Phys. J. B **93**, 74 (2020).
[21] H. Touchette, The large deviation approach to statistical mechanics, Phys. Rep. **478**, 1 (2009).
[22] J. P. Garrahan, R. L. Jack, V. Lecomte, E. Pitard, K. van Duijvendijk, and F. van Wijland, Dynamical first-order phase transition in kinetically constrained models of glasses, Phys. Rev. Lett. **98**, 195702 (2007).
[23] N. Tizón-Escamilla, C. Pérez-Espigares, P. L. Garrido, and P. I. Hurtado, Order and symmetry breaking in the fluctuations of driven systems, Phys. Rev. Lett. **119**, 090602 (2017).
[24] C. P. Royall, F. Turci, and T. Speck, Dynamical phase transitions and their relation to structural and thermodynamic aspects of glass physics, J. Chem. Phys. **153**, 090901 (2020).
[25] R. Chetrite and H. Touchette, Nonequilibrium Markov processes conditioned on large deviations, Ann. Henri Poincaré **16**, 2005 (2015).
[26] R. L. Jack and P. Sollich, Effective interactions and large deviations in stochastic processes, Eur. Phys. J. Special Topics **224**, 2351 (2015).
[27] U. Ray, Garnet Kin-Lic Chan, and D. T. Limmer, Exact fluctuations of nonequilibrium steady states from approximate auxiliary dynamics, Phys. Rev. Lett. **120**, 210602 (2018).
[28] L. Tociu, É. Fodor, T. Nemoto, and S. Vaikuntanathan, How dissipation constrains fluctuations in nonequilibrium liquids: Diffusion, structure, and biased interactions, Phys. Rev. X **9**, 041026 (2019).
[29] A. Das and D. T. Limmer, Nonequilibrium design strategies for functional colloidal assemblies, Proc. Natl. Acad. Sci. U.S.A. **120**, e2217242120 (2023).
[30] A. Lamtyugina, Y. Qiu, E. Fodor, A. R. Dinner, and S. Vaikuntanathan, Thermodynamic control of activity patterns in cytoskeletal networks, Phys. Rev. Lett. **129**, 128002 (2022).
[31] E. Fodor, R. L. Jack, and M. E. Cates, Irreversibility and biased ensembles in active matter: Insights from stochastic thermodynamics, Annu. Rev. Condens. Matter Phys. **13**, 215 (2022).
[32] F. Cagnetta, F. Corberi, G. Gonnella, and A. Suma, Large fluctuations and dynamic phase transition in a system of self-propelled particles, Phys. Rev. Lett. **119**, 158002 (2017).
[33] S. Whitelam, K. Klymko, and D. Mandal, Phase separation and large deviations of lattice active matter, J. Chem. Phys. **148**, 154902 (2018).
[34] T. GrandPre, K. Klymko, K. K. Mandadapu, and D. T. Limmer, Entropy production fluctuations encode collective behavior in active matter, Phys. Rev. E **103**, 012613 (2021).
[35] T. Nemoto, E. Fodor, M. E. Cates, R. L. Jack, and J. Tailleur, Optimizing active work: Dynamical phase transitions, collective motion, and jamming, Phys. Rev. E **99**, 022605 (2019).
[36] Y.-E. Keta, E. Fodor, F. van Wijland, M. E. Cates, and R. L. Jack, Collective motion in large deviations of active particles, Phys. Rev. E **103**, 022603 (2021).
[37] T. Agranov, M. E. Cates, and R. L. Jack, Tricritical behavior in dynamical phase transitions, Phys. Rev. Lett. **131**, 017102 (2023).
[38] L. Caprini, U. Marini Bettolo Marconi, and A. Puglisi, Spontaneous velocity alignment in motility-induced phase separation, Phys. Rev. Lett. **124**, 078001 (2020).
[39] L. Caprini, C. Maggi, and U. Marini Bettolo Marconi, Collective effects in confined active Brownian particles, J. Chem. Phys. **154**, 244901 (2021).
[40] M. Casiulis and D. Levine, Emergent synchronization and flocking in purely repulsive self-navigating particles, Phys. Rev. E **106**, 044611 (2022).
[41] See Supplemental Material at http://link.aps.org/supplemental/10.1103/PhysRevLett.134.038301, which includes Refs. [42–44] for movies and details on numerical simulations.
[42] W. Mickel, S. C. Kapfer, G. E. Schröder-Turk, and K. Mecke, Shortcomings of the bond orientational order parameters for the analysis of disordered particulate matter, J. Chem. Phys. **138**, 044501 (2013).
[43] V. Ramasubramani B. D. Dice, E. S. Harper, M. P. Spellings, J. A. Anderson, and S. C. Glotzerfreud: A software suite for high throughput analysis of particle simulation data, Comput. Phys. Commun. **254**, 107275 (2020).
[44] V. Lecomte and J. Tailleur, A numerical approach to large deviations in continuous time, J. Stat. Mech. (2007) P03004.
[45] B. Wittich and U. K. Deiters, The influence of the simulation box geometry in solid-state molecular simulations: Phase behaviour of lithium iodide in a dynamic Monte Carlo simulation, Mol. Simul. **36**, 364 (2010).
[46] G. Zhang, F. H. Stillinger, and S. Torquato, Probing the limitations of isotropic pair potentials to produce ground-state structural extremes via inverse statistical mechanics, Phys. Rev. E **88**, 042309 (2013).
[47] W. D. Piñeros and T. M. Truskett, Designing pairwise interactions that stabilize open crystals: Trunc. square and trunc. hex. lattices, J. Chem. Phys. **146**, 144501 (2017).
[48] C. Giardinà, J. Kurchan, and L. Peliti, Direct eval. of large-deviation functions, Phys. Rev. Lett. **96**, 120603 (2006).
[49] T. Nemoto, F. Bouchet, R. L. Jack, and V. Lecomte, Population-dynamics method with a multicanonical feedback control, Phys. Rev. E **93**, 062123 (2016).

[50] R. Hurtado-Gutiérrez, F. Carollo, C. Pérez-Espigares, and P. I. Hurtado, Building continuous time crystals from rare events, Phys. Rev. Lett. **125**, 160601 (2020).
[51] G. Briand, M. Schindler, and O. Dauchot, Spontaneously flowing crystal of self-propelled particles, Phys. Rev. Lett. **120**, 208001 (2018).
[52] L. Berthier, E. Flenner, and G. Szamel, Glassy dynamics in dense systems of active particles, J. Chem. Phys. **150**, 200901 (2019).
[53] R. Mandal, P. J. Bhuyan, P. Chaudhuri, C. Dasgupta, and M. Rao, Extreme active matter at high densities, Nat. Commun. **11**, 2581 (2020).
[54] P. K. Morse, S. Roy, E. Agoritsas, E. Stanifer, E. I. Corwin, and M. L. Manning, A direct link between active matter and sheared granular systems, Proc. Natl. Acad. Sci. U.S.A. **118**, e2019909118 (2021).
[55] E. Tjhung and L. Berthier, Analogies between growing dense active matter and soft driven glasses, Phys. Rev. Res. **2**, 043334 (2020).
[56] A. Ninarello, L. Berthier, and D. Coslovich, Models and algorithms for the next generation of glass transition studies, Phys. Rev. X **7**, 021039 (2017).
[57] C. Brito, E. Lerner, and M. Wyart, Theory for swap acceleration near the glass and jamming transitions for continuously polydisperse particles, Phys. Rev. X **8**, 031050 (2018).
[58] V. F. Hagh, S. R. Nagel, A. J. Liu, M. L. Manning, and E. I. Corwin, Transient learning degrees of freedom for introducing function in materials, Proc. Natl. Acad. Sci. U.S.A. **119**, e2117622119 (2022).
[59] V. Bolton-Lum, R. C. Dennis, P. Morse, and E. Corwin, The ideal glass and the ideal disk packing in two dimensions, arXiv:2404.07492.
[60] M. L. Manning, Essay: Collections of deformable particles present exciting challenges for soft matter and biological physics, Phys. Rev. Lett. **130**, 130002 (2023).
[61] H. Sakaguchi and Y. Kuramoto, A soluble active Rotater model showing phase transitions via mutual entertainment, Prog. Theor. Phys. **76**, 576 (1986).
[62] K. P. O'Keeffe, H. Hong, and S. H. Strogatz, Oscillators that sync and swarm, Nat. Commun. **8**, 1504 (2017).
[63] B. Adorjani, A. Libal, C. Reichhardt, and C. J. O. Reichhardt, Motility induced phase separation and frustration in active matter swarmalators, Phys. Rev. E **109**, 024607 (2024).
[64] S. Whitelam, D. Jacobson, and I. Tamblyn, Evolutionary reinforcement learning of dynamical large deviations, J. Chem. Phys. **153**, 044113 (2020).
[65] A. Das, D. C. Rose, J. P. Garrahan, and D. T. Limmer, Reinforcement learning of rare diffusive dynamics, J. Chem. Phys. **155**, 134105 (2021).
[66] J. Yan, H. Touchette, and G. M. Rotskoff, Learning nonequilibrium control forces to characterize dynamical phase transitions, Phys. Rev. E **105**, 024115 (2022).
[67] W. D. Piñeros, version 2 Zenodo repository, 10.5281/zenodo.14588892
[68] W. D. Piñeros, https://github.com/CreditDefaultSwap/pulsating_active_matter_popdyn.

## End Matter

*Appendix A: Overlap distance in dense monodisperse systems*—To compute the overlap distance $\sigma_{\mathrm{ovx}}$ for a monodisperse crystal, we determine the maximum interparticle distance $r_m$ which minimizes repulsion between particles by minimizing their overlap. Monodispersity implies that all particles have the same phase $\theta_i = \theta$. For arrested states ($\dot{\theta} = 0$), the noiseless phase dynamics [Eq. (3)] reduces to

$$\omega = n_n \mu_\theta \partial_\theta U(r, \theta), \tag{A1}$$

where $n_n$ is the number of contact neighbors, which defines an implicit function $r = r(\theta)$. Assuming hexagonal packing ($n_n = 6$) and maximizing with respect to $\theta$, we find $\theta_m \simeq 0.562$ and deduce $r(\theta_m) \simeq 0.845$. The overlap distance follows as $\sigma_{\mathrm{ovx}} = 2\sigma_m - r_m \simeq 0.133$, where $\sigma_m = [1 + \lambda \sin(\theta_m)]/[2(1+\lambda)]$ is the optimal particle radius [Eq. (1)].

*Appendix B: Structural analysis of biased configurations*—To systematically characterize the structural configurations emerging under bias, we measure the orientational order parameter $\Psi_k$ defined as

$$\Psi_k = \frac{1}{N} \left\langle \sum_{j=1}^{N} \sum_{l=1}^{n_j} e^{ik\alpha_{jl}} \right\rangle_{\mathrm{gb}}, \tag{B1}$$

where $n_j$ is the number of nearest neighbors of particle $j$ and the integer $k$ refers to the degree of orientational order. The orientation angle $\alpha_{jl}$ is defined in terms of the distance vector between two neighboring particles $(j, k)$ relative to a fixed axis. We choose to consider $k = \{4, 6\}$, and we employ the weighed Voronoi method to evaluate $\Psi_{4/6}$ [42,43]. The system goes from hexagonal-like to squarelike structures as $L/\ell$ varies from arrest ($L/\ell \simeq 5$, high $\Psi_4$, and low $\Psi_6$) to cycling and intermittent states ($L/\ell \neq 5$, high $\Psi_6$, and low $\Psi_4$) [Fig. 5(a)].

Interactions between particle phases $\theta_i$ take place whenever particles are in contact ($a_{ij} \leq 1$), so that structural order can emerge only via the following two conditions: (i) low particle polydispersity (i.e., phase homogeneity) and (ii) persistent neighborhood of particle contacts. The latter accounts for the fact that irregular contact profiles (e.g., via structural defects) alter the local phase dynamics and promote polydispersity. In contrast, for passive particles with fixed sizes, interparticle distance alone suffices to determine structural order.

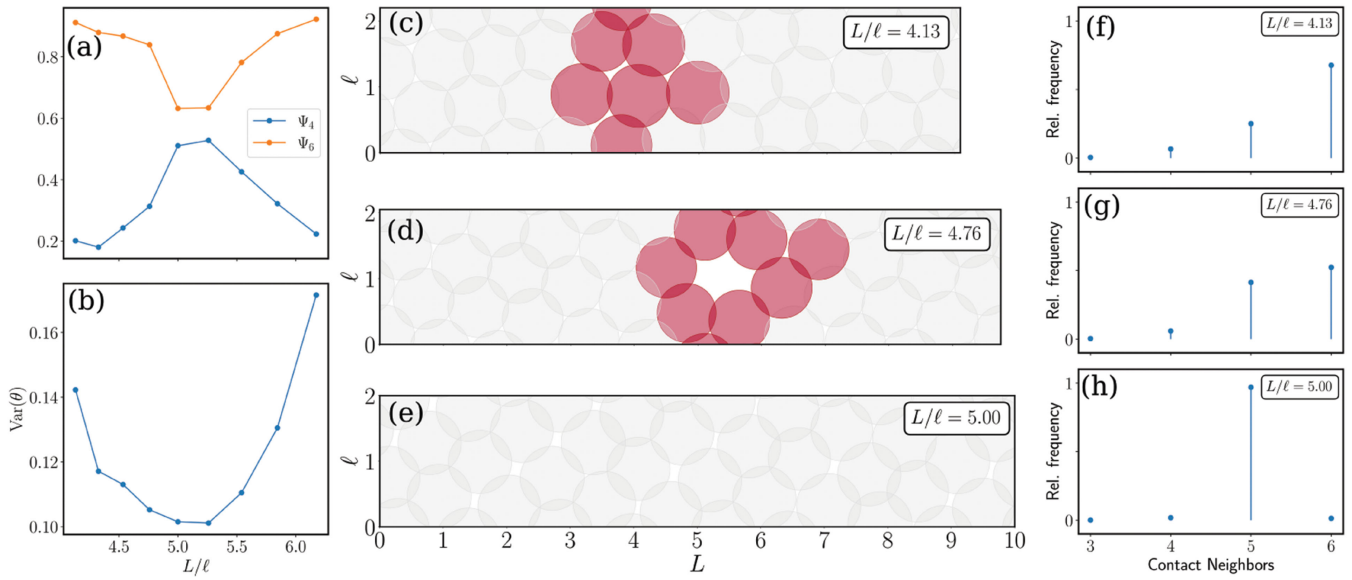


FIG. 5. (a) Orientational order parameters $\Psi_{4/6}$ and (b) phase variance $\mathrm{Var}(\theta)$ in ensembles biased by global order [Eq. (9)], as functions of the box geometry $L/\ell$ for $s = -6$. (c)–(e) Corresponding snapshots of biased configurations, identical to Fig. 1, here colored by the number of contact neighbors. For (c) and (d), red indicates particles with five contact neighbors or less and gray for six neighbors. For (e), gray indicates particles in contact with five neighbors. (f)–(h) Histogram in time of the number of contacts estimated from biased trajectories, with the same parameters as in (c)–(e).

To evaluate the statistics of particle polydispersity, we first measure the phase variance

$$\mathrm{Var}(\theta) = \frac{1}{N}\left\langle \sum_{i=1}^{N} (\theta_i - \theta_m)^2 \right\rangle_{\mathrm{gb}} \tag{B2}$$

for realizations where the average phase $\theta_m = (1/N)\sum_{j=1}^{N}\theta_j$ is approximately the same for all states (either arrested, intermittent, or cycling). We find that $\mathrm{Var}(\theta)$ is lowest for arrest ($L/\ell = 5$) and higher for the intermittent and cycling states ($L/\ell = 4.13$ and 6.17, respectively) [Fig. 5(b)]. This result indicates that arrest features a more homogeneous phase distribution (i.e., lower polydispersity) than intermittent or cycling states.

Second, we display the contact profiles, given by the number of contact neighbors per particle [Figs. 5(c)–5(e)] and estimate their persistence in time via histograms of the number of contacts from the corresponding biased trajectories [Figs. 5(f)–5(h)]. For intermittent and cycling states, histograms reveal a majority of six-neighbor contacts, along with noticeable contributions from contacts with five or fewer neighbors [Figs. 5(f) and 5(g)]: This result hints at the presence of defects in a hexagonal packing structure. In contrast, five-neighbor contacts predominate for arrest [Fig. 5(h)], indicating a persistent, regular structure, albeit with a nonhexagonal packing. Indeed, the arrested structure conforms to an elongated honeycomb crystal, as shown in Fig. S4 of [41].

In all, the structural analysis supports that arrest is associated with a regular packing configuration, whereas intermittent and cycling states feature some defective and nonpersistent configurations.